



A crucial role of enhanced Volmer-Tafel mechanism in improving the electrocatalytic activity *via* synergetic optimization of host, interlayer, and surface features of 2D nanosheets

Hyun Kyu Kim^{a,1}, Haeseong Jang^{b,1}, Xiaoyan Jin^{a,*}, Min Gyu Kim^{b,*}, Seong-Ju Hwang^{a,*}

^a Department of Materials Science and Engineering, College of Engineering, Yonsei University, Seoul 03722, Republic of Korea

^b PLS-II Beamline Division, PLS-II Department, Pohang Accelerator Laboratory (PAL), Pohang University of Science and Technology (POSTECH), Pohang 37673, Republic of Korea

ARTICLE INFO

Keywords:

Host–guest co-engineering
Surface activation
Electrocatalysts
Volmer–Tafel mechanism
Electrochemical active surface area

ABSTRACT

High-performance electrocatalysts have attracted growing interest because of their crucial roles in renewable energy technologies. In this study, the host, interlayer, and surface features of electrocatalytically-active 2D nanosheets (NSs) are systematically controlled with the synergetic combination of host–guest co-engineering and surface modification to develop a novel synthetic strategy for efficient electrocatalysts. Molecular-level control of interfacial electronic coupling and surface reactivity can be achieved by the self-assembly of MoS₂/RuO₂ NS mixtures with variable-sized tetraalkylammonium cations and subsequent thermal aging. The resulting optimization of the operation mechanisms of restacked MoS₂/RuO₂ NSs effectively improves the electrocatalyst functionality for hydrogen evolution reaction (HER). The extensive modifications of diverse structural and morphological parameters allow the elucidation of a linear correlation between electrochemical active surface area and HER overpotential. Systematic *in-situ* spectroscopic analyses clearly demonstrate the crucial role of enhanced Volmer–Tafel mechanism in improving the electrocatalytic activity *via* enhancement of proton adsorption and interfacial electron transfer.

1. Introduction

High-performance electrocatalysts have received growing attention because of the crucial role of electrolytic reactions in emerging renewable energy technologies, such as fuel cells, water electrolyzers, and metal–O₂ batteries [1–5]. The high electrochemical and catalytic activities of two-dimensional (2D) inorganic nanosheets (NSs), such as MoS₂ and layered double hydroxides (LDHs) render these materials useful building blocks for exploring novel efficient hybrid electrocatalysts [6,7]. For example, the intercalative hybridization of various guest species can provide useful means to improve the functionality of 2D nanostructured electrocatalysts [8]. Although the conventional intercalation reaction of guest species into 2D host lattices only allows control of the interlayer spacing [9], the self-assembly of heterogeneous host NSs with variable-sized intercalant species enables to simultaneous manipulation of the host and guest layers [10,11]. Since the characteristics of the host and guest species, such as their chemical compositions,

stacking thicknesses, and defect contents, determine their electrical conductivities, redox capabilities, and mass transfer properties, respectively [12], the molecular-level control of host and interlayer features achieved by the self-assembly of colloidal NS mixtures is expected to be effective in optimizing their catalytic activities *via* an improvement in their charge and mass transport kinetics. Considering the vast library of colloidal mixtures of exfoliated inorganic NSs, such as graphene, transition metal dichalcogenides (TMDs), transition metal oxides (TMOs), and transition metal carbides (TMCs) that have been reported to date [10,11,13–16], there is significant potential for the preparation of efficient 2D mixed host-based hybrid electrocatalysts with diverse host–guest couples. In addition to host–guest co-engineering, the post-synthesis treatment of restacked NSs is expected to further improve their catalytic activities *via* surface modification [17–22]. For example, the high surface reactivity of ultrathin monolayer 2D NSs bearing numerous coordinatively-unsaturated surface sites could allow modification of the surface bonding nature *via* a short thermal aging step

* Corresponding authors.

E-mail addresses: xyjin313@yonsei.ac.kr (X. Jin), mngkim@postech.ac.kr (M.G. Kim), hwangsju@yonsei.ac.kr (S.-J. Hwang).

¹ These authors contributed equally to this work.

in standard glassware. Thus, the simultaneous control of host, interlayer, and surface properties can provide novel synthetic routes to high-performance 2D NS-based hybrid electrocatalysts through optimization of contributing operation mechanism [23,24]. Furthermore, it is worth noting that the resulting heterolayered nanohybrids with elaborately-tailored guest and host layers can be used as appropriate model compounds for elucidating the effects of structural/morphological parameters, such as the interlayer distance, the stacking structure, the defect content, and the surface area, on the electrocatalytic activity. Moreover, the systematic *in-situ* spectroscopic analyses of these model compounds can provide valuable opportunities to elucidate crucial mechanism for optimizing the electrocatalyst performance of 2D nanosheets. However, at the time of this submission, we are unaware of any other study related to the systematic molecular-level control of host, interlayer, and surface features, and simultaneous *in-situ* spectroscopic analysis to establish crucial operation mechanism and governing design factors for efficient 2D nanostructured electrocatalysts.

Thus, we herein report the elucidation of dominant operation mechanism and design factors for optimizing the electrocatalytic activity of 2D nanosheets through the synergetic control of their host, interlayer, and surface features, providing a novel lattice engineering route to high-performance hybrid electrocatalysts. An electrostatically-driven self-assembly of a colloidal mixture of MoS₂/RuO₂ NSs with variable-sized organic cations followed by thermal aging in a standard glassware reactor is carried out with the aim of producing 2D heterolayered organic–MoS₂–RuO₂ hybrid electrocatalysts with finely-controlled defect, stacking, and surface structures. Along with a series of *in-situ* spectroscopic analyses, the systematic control of various structural and morphological parameters of the restacked NSs is also carried out to investigate their influences on the electrocatalytic performances and chemical bonding natures, and to elucidate design factors and underlying mechanisms involved in the generation of high-performance 2D electrocatalysts.

2. Experimental

2.1. Sample preparation

As building blocks for the organic–MoS₂–RuO₂ nanohybrids, monolayered 2D MoS₂ and RuO₂ NSs were synthesized by the exfoliation of the pristine MoS₂ and NaRuO₂, respectively [25,26]. Specifically, the exfoliated 2D MoS₂ NS was synthesized by the lithiation–hydroxylation reaction of bulk MoS₂ [25], whereas the exfoliated RuO₂ NS was obtained by the organic intercalation of protonated Na_{0.2}RuO₂ [26]. The negative surface charges of exfoliated MoS₂ and RuO₂ NSs were verified by the zeta potential measurement (Fig. S1, Supporting Information). Mixing of the exfoliated MoS₂ and RuO₂ NSs yielded stable colloidal mixtures (Fig. S1, Supporting Information), which were used as precursors for synthesizing the mixed 2D host nanohybrids. A series of organic–MoS₂–RuO₂ nanohybrids (i.e., **TEMR7**, **TPrMR7**, **TBMR7**, **TPeMR7**, and **THMR7**) were synthesized by self-assembly between the colloidal mixture of anionic RuO₂/MoS₂ NSs (7% molar ratio) and tetraethylammonium (TEA), tetrapropylammonium (TPrA), tetrabutylammonium (TBA), tetrapentylammonium (TPeA), and tetrahexylammonium (THA), respectively, in a molar ratio of 1:1. In contrast, the use of tetramethylammonium (TMA) ions as intercalants was ineffective in inducing the self-assembly process. Subsequently, the flocculated precipitate was thoroughly washed with distilled water, restored by high-speed centrifugation, and then freeze-dried. To probe the effects of host mixing and thermal aging on the nanohybrid functionalities, additional TBA–MoS₂–RuO₂ nanohybrids were synthesized with RuO₂ molar ratios of 7%, 9%, and 11% (denoted as **TBMR7**, **TBMR9**, and **TBMR11**, respectively). Beyond 11%, the homogeneously-stacked single-phase nanohybrids with higher RuO₂ NS contents could not be obtained due to the phase separation of the restacked MoS₂ and RuO₂ NSs (Fig. S2, Supporting Information). For

surface activation of the as-prepared nanohybrids, the **TBMR7**, **TBMR9**, and **TBMR11** materials were subjected to thermal aging at 70–90 °C for 1–3 h in standard a glassware reactor.

2.2. Characterization

The crystal structures of the materials were determined by powder X-ray diffraction (XRD) measurements (Rigaku Ultima IV, $\lambda = 1.5418 \text{ \AA}$, 25 °C). High resolution-transmission electron microscopy (HR-TEM, JEOL JEM-200 microscope with an accelerating voltage of 200 kV) and field emission-scanning electron microscopy (FE-SEM, JEOL JSM-7001F microscope) were employed to characterize the stacking structures and crystal morphologies of the present nanohybrids. The spatial elemental distribution of the present nanohybrids was examined with energy dispersive spectrometry (EDS)–elemental mapping analysis [27]. The electronic configurations and local atomic arrangements of the nanohybrids were investigated with *in-situ* and *ex-situ* X-ray absorption near-edge structure/extended X-ray absorption fine structure (XANES/EXAFS) spectroscopy. All XANES/EXAFS data were collected in transmission mode at beamlines 8 C and 10 C of the Pohang Accelerator Laboratory (PAL, Pohang) in Korea. Data processing of the XANES/EXAFS spectra was carried out according to a previously-reported standard procedure [28]. The micro-Raman measurements were performed using a Horiba Jobin-Yvon LabRam Aramis spectrometer to probe the structure types and chemical bonding natures of the nanohybrids. A diode laser with a radiation wavelength of 514.5 nm was employed as an excitation source for Raman spectroscopy. *In-situ* surface enhanced Raman scattering (SERS) analyses were carried out using a Horiba Jobin-Yvon LabRam Aramis instrument with an Ar-ion laser beam ($\lambda = 514 \text{ nm}$), and by loading the electrocatalyst materials onto the Au nanoparticle-based SERS substrate. The interfacial charge transfers and chemical environments of the nanohybrids were probed by X-ray photoelectron spectroscopy (XPS) analysis (Thermo VG, U.K., Al K α).

2.3. Electrocatalytic activity measurement

The nanohybrids were examined for their potential application in the HER by measuring their linear sweep voltammetry (LSV) curves using an RRDE-3A (ALS) as a rotator and an Ivium analyzer. The LSV data were obtained by employing a three-electrode system with a Pt wire counter electrode and a saturated calomel reference electrode (SCE, sat. KCl). The measured potentials were normalized with respect to the reversible hydrogen electrode (RHE) according to the following equation: $E_{\text{RHE}} = E_{\text{SCE}} + 0.256 \text{ V}$. The working electrode was fabricated by loading 10 μL of the electrode ink onto a glassy carbon, which was subjected to oven-drying. The electrode ink was composed of the active material (2 mg) dispersed in a mixed solution of Milli-Q water (0.8 mL), isopropyl alcohol (0.2 mL), and a 5 wt% Nafion solution (20 μL). After purging with N₂ gas for 0.5 h, the LSV measurements were carried out at a scan rate of 5 mV sec^{−1} using a 0.5 M H₂SO₄ electrolyte. To remove the H₂ bubbles from the electrode surface, the working electrode was rotated at 1600 rpm during the electrochemical measurements. The electrocatalytic stabilities of the present nanohybrids were probed with chronopotentiometric curves. The charging current density was measured as a function of the scan rate by cyclic voltammetry (CV) in the non-Faradaic region (0.21–0.31 V vs. RHE). The electrochemical impedance spectroscopy (EIS) measurements were performed at −0.12 V (vs. RHE) over a frequency range of 0.1–100000 Hz.

3. Result and discussion

3.1. Molecular-level control of interlayer distance between restacked MoS₂ and RuO₂ NSs

To elucidate the effects of host and interlayer features on the

electrocatalyst functionalities of the restacked nanohybrids, a range of intercalative organic–MoS₂–RuO₂ nanohybrids with various RuO₂/MoS₂ ratios and interlayer distances were synthesized by the electrostatically-driven self-assembly between colloidal mixture of anionic MoS₂/RuO₂ NSs and quaternary tetraalkylammonium cations (Fig. 1a). The formation of interstratified hybrid structure of the

restacked MoS₂ and RuO₂ monolayers was evidenced by cross-sectional TEM analysis (Fig. 1b). Upon increasing the intercalant size, the distance between the lattice fringe gradually increases, providing strong evidence that effective tailoring of the interlayer distance can be achieved. As shown in the powder XRD patterns (Fig. 1c), all the nanohybrids presented herein displayed well-developed (00 *l*) reflections in the low

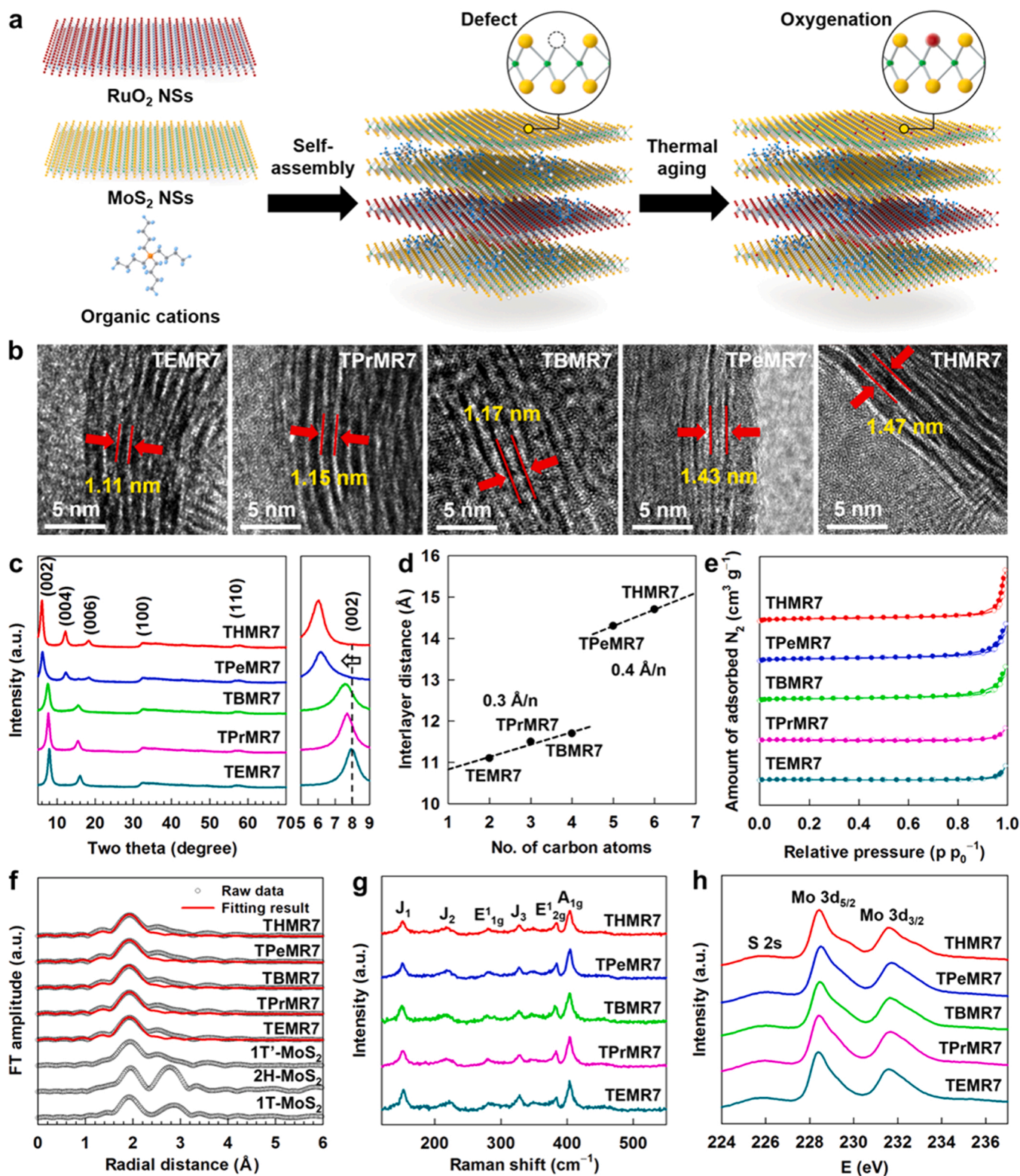


Fig. 1. (a) Schematics for host–guest co-engineering and thermal aging route. (b) TEM, (c) powder XRD, (d) plot of interlayer distance vs. carbon number, (e) N₂ adsorption–desorption isotherms, (f) Mo K-edge FT-EXAFS, (g) micro-Raman, and (h) Mo 3d XPS of organic–MoS₂–RuO₂ nanohybrids and several references.

angle region, confirming the formation of the layer-by-layer-ordered stacking structure of homogeneously-mixed MoS₂ and RuO₂ NSs with intercalated tetraalkylammonium cations. An increase in the intercalant size led to the gradual shift of (00 l) peaks toward the low-angle side and the change of XRD features in the two theta region of 10–20°, certifying the molecular-level control of the interlayer distance between the restacked MoS₂ and RuO₂ monolayers (Table S1, Supporting Information). In addition, the increase of structural anisotropy caused by the intercalation of bulky organic cations makes visible (006) reflection for **TPeMR7** and **THMR7** nanohybrids, as well-documented for organic-intercalation compounds [29]. As can be seen clearly from Fig. 1d, there is a distinct discontinuity of slope between **TBMR7** and **TPeMR7** in the plot of interlayer distance vs. carbon number (i.e., carbon number of each alkyl chain in guest tetraalkylammonium cations). Such a slope discontinuity reflects the abrupt change of the packing structure of intercalated tetraalkylammonium cations. The increase of alkyl chain length in tetraalkylammonium (i.e. the increase of guest volume) leads to the denser packing of these guest species. The resulting tight packing of larger tetraalkylammonium species in the confined interlayer space increases the tilting angle of packed alkyl chain toward steeper angle, resulting in the abrupt increase of interlayer spacing upon the intercalation, as reported previously [10]. In addition to the (00 l) reflections, the in-plane (100) and (110) reflections of the MoS₂ phase were discernible, confirming retention of the layered MoS₂ structure after hybridization. Due to the low content of RuO₂ NSs, no RuO₂-related in-plane reflections appeared in the XRD patterns.

In the FE-SEM images (Fig. S3, Supporting Information), all materials under investigation demonstrated a highly porous morphology composed of a house-of-cards-type stacking structure, which is common to 2D NS crystallites [7,13]. The nanoscale hybridization between MoS₂ and RuO₂ NSs was obviously verified by EDS–elemental mapping analysis showing the homogeneous distribution of Mo, S, Ru, and O elements in the entire region of the present **TBMR7** nanohybrid (Fig. S4, Supporting Information). The formation of a loosely-packed porous structure was further confirmed by N₂ adsorption–desorption isotherm measurements. The marked N₂ adsorption occurred for all nanohybrids with distinct hysteresis being observed in each case (Fig. 1e). According to the IUPAC classification, the observed isotherm behaviors of the present nanohybrids are classified as Brunauer–Deming–Deming–Teller (BDDT)-type IV shape isotherms and H3-type weak hysteresis loop, indicating the aggregation of plate-like particles with slit-shaped mesopores [30]. It was also found that an enlargement in the interlayer space gave rise to a notable enhancement in the N₂ adsorption and hysteresis properties, suggesting an increase in porosity. The surface area calculation based on the Brunauer–Emmett–Teller (BET) equation clearly demonstrated a gradual increase in the surface area with enlargement of the guest size. Among the present materials, the **THMR7** nanohybrid with the largest basal spacing possessed the largest surface area of 37.2 m² g^{−1}, thereby highlighting the beneficial effect of basal expansion on the porosity of the restacked NSs (Table S1, Supporting Information).

According to the Mo K-edge and Ru K-edge XANES analyses (Fig. S5, Supporting Information), all nanohybrids displayed nearly identical spectral features to those of the MoS₂ and RuO₂ NS precursors, indicating retention of these original structures upon hybridization with the organic intercalants. The 1 T'-MoS₂-type local atomic arrangement of the MoS₂ component in the present nanohybrids was further supported by Mo K-edge EXAFS analysis. More specifically, the nanohybrids examined herein exhibited typical Fourier-transformed (FT) features of the 1 T'-MoS₂ phase, including three peaks corresponding to (Mo–S) and two different (Mo–Mo) shells at ~1.8, ~2.4, and ~2.9 Å, respectively (Fig. 1f) [31]. The observed spectral features are clearly distinguishable from those of the 2 H- and 1 T-MoS₂ phases, thereby confirming stabilization of the metallic 1 T'-MoS₂ phase upon restacking with bulky organic cations [32,33]. The curve fitting analysis for the Mo K-edge EXAFS spectra clearly demonstrated that the increase in the

interlayer distance led to a gradual lowering of the coordination number (CN) for the (Mo–S) bonding pair, thereby suggesting the presence of an increased number of sulfur vacancies (Table S2, Supporting Information). This result provides strong evidence for the controllability of the defect content upon variation in the guest size. The observed increase of the crystal defect content can be ascribed to the enhancement in the crystal strain upon lattice expansion [34,35]. In addition, stabilization of the 1 T'-MoS₂ phase was further verified by micro-Raman spectroscopy showing the characteristic phonon lines of the 1 T'-MoS₂ phase (J₁, J₂, and J₃) and the 1 T'/2 H-MoS₂ phase (E_{1g}, E_{2g}, and A_{1g}) for the nanohybrids (Fig. 1g) [36,37]. Furthermore, Mo 3d XPS analysis provided additional confirmation regarding the increased stability of the 1 T'-MoS₂ phase upon expanding the interlayer distance. As depicted in Fig. 1h and S6 of Supporting Information, the 1 T'-MoS₂/2 H-MoS₂ ratio became larger upon increasing the interlayer distance (i.e., 0.80 for **TEMR7**, 0.84 for **TPrMR7**, 0.89 for **TBMR7**, 0.96 for **TPeMR7**, and 1.04 for **THMR7**). This result therefore confirms that stabilization of the 1 T'-MoS₂ phase took place upon increasing the size of the guest species.

3.2. Effect of interlayer distance on the electrocatalyst functionality of restacked MoS₂–RuO₂ NSs

As presented the LSV data of Fig. 2a, the restacked nanohybrids presented herein delivered promising and superior HER electrocatalyst functionalities over those of the MoS₂ NS and RuO₂ NS precursors and their physical mixture, thereby providing clear evidence for the beneficial effect of nanoscale hybridization on the electrocatalytic performance of restacked NSs (Fig. S7, Supporting Information). It is worth noting that variation of the interlayer distance has a profound effect on the HER performances of the nanohybrids. Among the various materials under investigation, **TBMR7** displayed the smallest overpotential of 145 mV at 10 mA cm^{−2} with an increased current density (Fig. 2b and Table S3 of Supporting Information). This observation clearly demonstrates that restacking with TBA offers an optimal interlayer space for improving the HER activity of the restacked MoS₂ and RuO₂ NSs, which in turn leads to an improvement in the electrocatalyst functionality. Beyond this optimal composition, a further basal expansion was found to degrade the electrocatalytic performance, which is in contrast to the previous reports showing an increase in the HER activity upon expanding the interlayer distances of 2D electrocatalyst NSs [38]. The beneficial effect of interlayer control on the HER kinetics of nanohybrids was further evidenced by the Tafel slope calculation. The **TBMR7** nanohybrid exhibited the smallest Tafel slope of 61.1 mV dec^{−1}, thereby confirming the successful optimization of the HER kinetics after restacking with TBA (Fig. 2c and Table S3 of Supporting Information). As can be seen clearly from the chronopotentiometric curve data (Fig. 2d), a stable electrocatalytic performance was achieved for **TBMR7** during the repeated tests, which is better than the stability of unhybridized MoS₂ NSs. This result further highlights the improved electrocatalytic stability resulting from the hybridization process. In addition, the FE-SEM and Mo K-edge EXAFS analyses were carried out for the **TBMR7** nanohybrid subjected to the stability test. As presented in Fig. S8 of Supporting Information, the original crystal structure, porous stacking morphology, and 1 T'-MoS₂ phase of this material remained unchanged after the stability test, providing additional confirmation for the excellent stability of this material. The exchange current densities (J₀) related to the kinetics of the charge transfer reactions were then calculated by extrapolating the Tafel plots to 0 mV. The **TBMR7** nanohybrid displayed a higher J₀ value than those of the other nanohybrids, confirming the most effective promotion of the HER activity upon restacking with TBA. The significant influence of the interlayer spacing on the electrochemical activity of the nanohybrid was also evidenced by electrochemical active surface area (ECSA) calculations based on the double-layer capacitance (C_{dl}) and the specific capacitance (C_s) [39]. More specifically, the CV measurements carried out in the potential window of 0.21–0.31 V (vs. RHE) allowed us to determine the specific

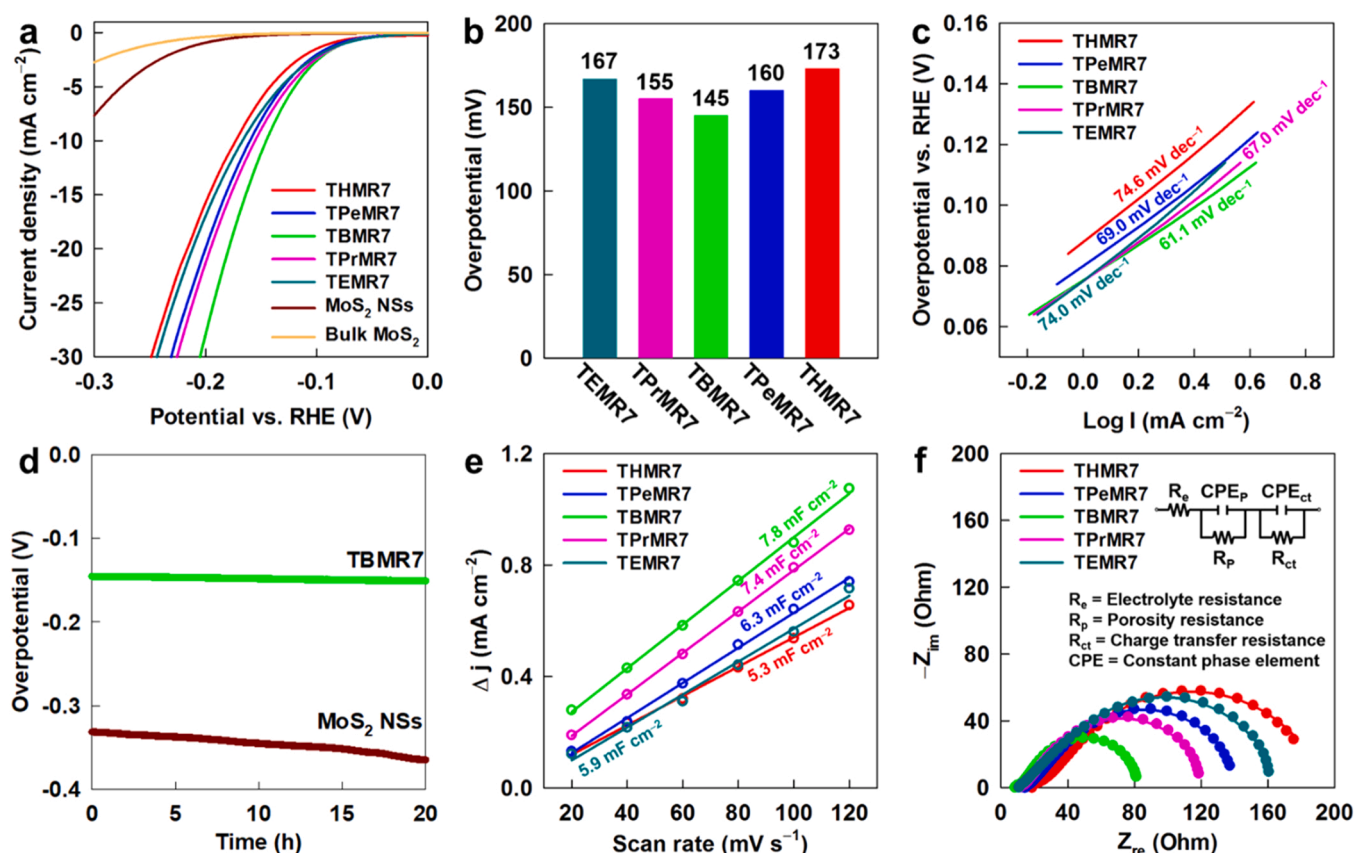


Fig. 2. (a) LSV curves of HER, (b) overpotential plot, (c) Tafel slope, (d) chronopotentiometric curves measured at 10 mA cm^{-2} , (e) plots of current density difference vs. scan rate, and (f) EIS data measured at -0.12 V (V vs. RHE) for organic-MoS₂-RuO₂ nanohybrids, MoS₂ NSs, and bulk MoS₂.

capacitance from the slopes of the charging current vs. the scan rate. A C_s of $35 \mu\text{F cm}^{-2}$ was assumed for a flat surface in acidic media [40]. The **TBMR7** showed a larger ECSA value of 15.8 cm^2 than those of the other homologues, confirming its highest electrochemical activity (Fig. 2e and Table S3 of Supporting Information). The trends in ECSA do not match well with the trends in surface area. Since the increase of surface area is achieved by the intercalation of bulky organic cations, the accompanying increase of electrochemically-inactive hydrophobic organic guest content and the lowering of surface hydrophilicity caused the depression of ECSA. Thus, the smaller ECSA of **THMR7** than **TBMR7** can be interpreted as a result of interplay between the beneficial effect of surface expansion and the detrimental effect of increased electrochemically-inactive component and increased hydrophobicity. The marked dependence of the charge transport property on the interlayer distance of the present nanohybrids was then verified by EIS. In the Nyquist plots measured at an applied potential of -0.12 V (vs. RHE), the nanohybrids demonstrated similar spectral features, with semicircles representing their charge transfer resistance (R_{ct}), as shown in Fig. 2f and Table S3 of Supporting Information. Among the present nanohybrids, **TBMR7** exhibited the smallest semicircle radius and the smallest R_{ct} of 61.5Ω , indicating that successful optimization of the charge transfer kinetics had been achieved upon restacking with TBA. Summarizing the above electrochemical results, it was apparent that the intermediate interlayer spacing achieved using the TBA intercalant gave optimal electrocatalytic performances and charge transfer properties for the restacked nanohybrids. This can be ascribed to the interplay between the beneficial effect of basal expansion (i.e., the increased surface area and enhanced mass transfer) and the accompanying detrimental effect (i.e., the weakening of electronic coupling between the restacked MoS₂ and RuO₂ NSs). Since the type of counter electrode was reported to affect the electrocatalyst functionality [41], additional HER activity tests were

carried out for the **TBMR7** nanohybrid using a graphite electrode as the counter electrode. As plotted in Fig. S9 of Supporting Information, the **TBMR7** nanohybrid showed very similar HER activity with nearly identical overpotential to that measured with Pt counter electrode, which allows to rule out the influence of counter electrode type on the obtained HER electrocatalyst performances of the present materials.

To verify the universal usefulness of the present host-guest co-engineering strategy, additional restacked nanohybrids were synthesized by restacking of homogeneously-mixed MoS₂ and reduced graphene oxide (rGO) NSs with TBA cations. As presented in Fig. S10 of Supporting Information, the restacked TBA-MoS₂-rGO nanohybrids displayed higher HER electrocatalyst activity over those of the MoS₂ NS and rGO NS precursors and their physical mixture, indicating the advantage of nanoscale hybridization in improving the electrocatalytic performance of restacked NSs. This result provides strong evidence for the versatile validity of the present strategy in exploring high-performance 2D nanostructured hybrid electrocatalysts.

3.3. Effect of host composition on the electrocatalyst functionality of restacked MoS₂-RuO₂ NSs

In addition to the interlayer property, the host layer composition was expected to significantly affect the electrocatalytic performance of the restacked nanohybrids. Thus, the effect of host composition was studied using several **TBMR7**, **TBMR9**, and **TBMR11** nanohybrids containing RuO₂/MoS₂ molar ratios of 7, 9, and 11 mol%, respectively. The homogeneous incorporation of RuO₂ NS into the heterolayered TBA-MoS₂ lattice was then verified by powder XRD analysis, which indicated the formation of single-phase **TBMR** nanohybrids. As presented in Fig. 3a, an increase in the RuO₂ content caused a slight but distinct displacement of the (001) peaks into high angle side, which was attributed to the

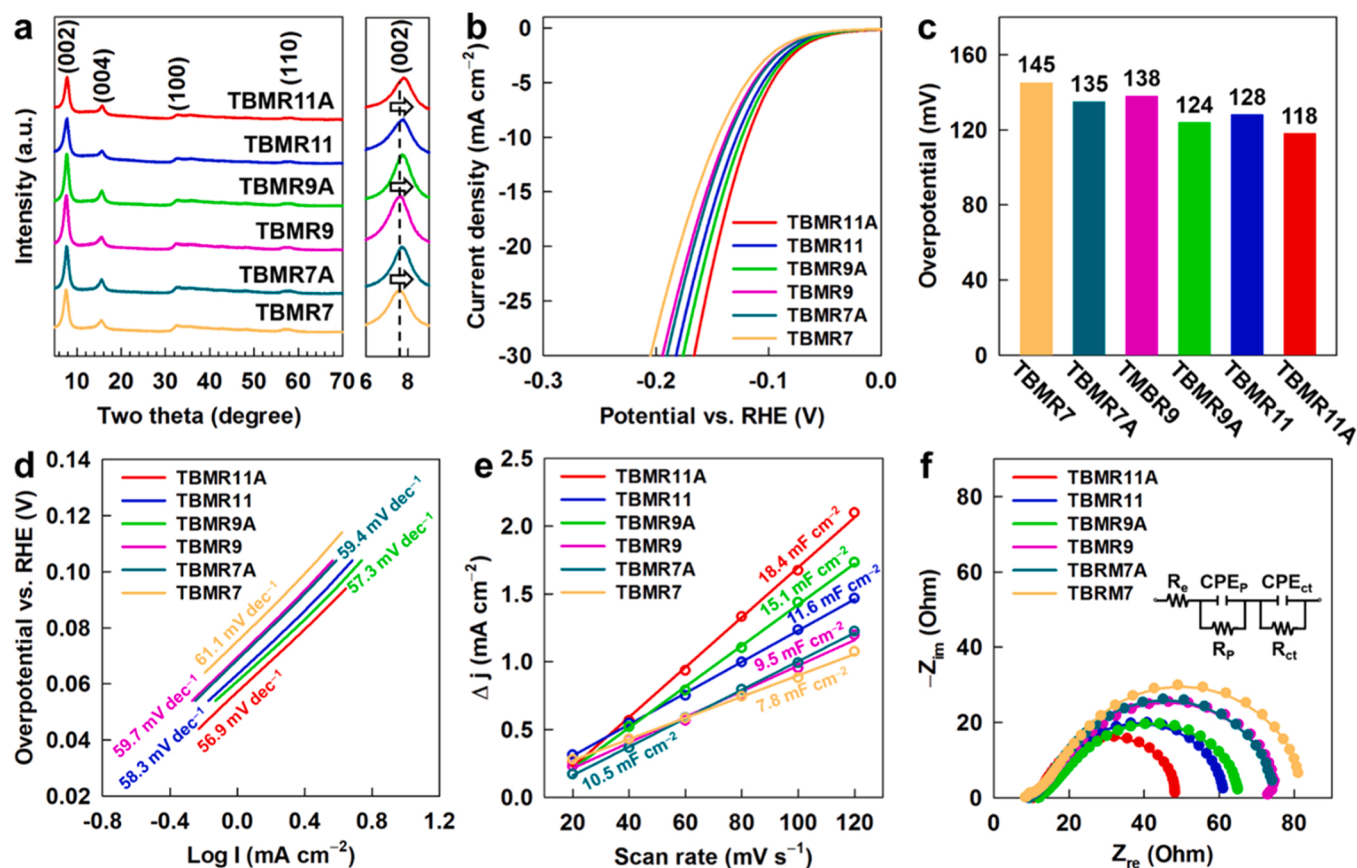


Fig. 3. (a) Powder XRD, (b) LSV curves of HER, (c) overpotential plot, (d) Tafel slope, (e) plots of current density difference vs. scan rate, and (f) EIS data measured at -0.12 V (V vs. RHE) for TBMR7, TBMR9, and TBMR11 nanohybrids before and after thermal aging.

replacement of the thinner RuO_2 NS (0.51 nm) for thicker MoS_2 NS (0.65 nm) [25,26,42]. Retention of the highly porous house-of-cards-type stacking structure upon variation in the RuO_2 NS content was confirmed by FE-SEM and N_2 adsorption-desorption isotherm measurements (Figs. S11 and S12, Supporting Information). According to the surface areas determined using the BET approach, the RuO_2 content had only a negligible influence on the surface area, with values of 31, 33, and $29 \text{ m}^2 \text{ g}^{-1}$ being obtained for the TBMR7, TBMR9, and TBMR11 nanohybrids, respectively.

The effects of the host composition on the HER activities of the TBMR nanohybrids were then examined by measuring the LSV curves (Fig. 3b). More specifically, an increase in the RuO_2 NS content improved the HER electrocatalytic activity with a lowering of the overpotential at a current density of 10 mA cm^{-2} , thereby emphasizing the effective role of the RuO_2 NS in enhancing the HER electrocatalytic performance. The TBMR11 nanohybrid delivered the best HER performance with the smallest overpotential of 128 mV (Fig. 3c and Table S3 of Supporting Information). However, beyond 11%, a further increase in the RuO_2 NS content resulted in phase separation of the restacked MoS_2 and RuO_2 NSs, which had a detrimental effect on the electrocatalyst performance of the resulting TBMR nanohybrids (Figs. S2 and S13, Supporting Information). The HER activity of the TBMR11 nanohybrid is a significantly superior result to that obtained for the physical mixture of the MoS_2 and RuO_2 NSs at the same composition (Fig. S7, Supporting Information). This result can be regarded as strong evidence for the beneficial effect of the nanoscale coupling between monolayer MoS_2 and RuO_2 NSs. The Tafel plot measurement for the TBMR nanohybrids clearly demonstrated that the incorporation of a RuO_2 NS promotes the HER kinetics with the lowering of Tafel slope (Fig. 3d and Table S3 of Supporting Information). Additionally, an increase in the RuO_2 content was found to be effective in increasing the ECSA to 23.4 cm^2 for

TBMR11 (Fig. 3e and Table S3 of Supporting Information), thereby confirming the enhanced electrochemical activity of the nanohybrid achieved by incorporation of the highly conductive RuO_2 NS. The beneficial effect of RuO_2 NS addition on the charge transfer kinetics was further verified by EIS analysis. As plotted in the Nyquist plots measured at -0.12 V (Fig. 3f and Table S3 of Supporting Information), an increased RuO_2 NS content reduced the diameter of the semicircle, indicated an improvement in the charge transfer properties [43]. The R_{ct} values for the present nanohybrids were determined to be 61.5, 55.4, and 44.3Ω for TBMR7, TBMR9, and TBMR11, respectively, indicating the advantageous effect of the RuO_2 NS on the charge transfer properties of the restacked nanohybrids. The improvement is mainly responsible for the enhanced HER activity observed upon the addition of the conductive RuO_2 NS.

3.4. Effect of thermal aging process on the electrocatalyst functionality of restacked MoS_2 - RuO_2 NSs

Judging from the high surface reactivity of ultrathin monolayer NSs with unusually high surface-to-volume ratios [44,45], the thermal aging treatment of restacked NSs at elevated temperatures was expected to improve their electrocatalyst performances via surface activation and an enhancement in the interfacial interaction between the restacked NSs. Thus, to examine the effect of aging on the electrocatalytic activity of the restacked NSs, the thermally-aged TBMR7A, TBMR9A, and TBMR11A nanohybrids were synthesized by aging the corresponding as-prepared nanohybrids at 70°C for 1 h. According to powder XRD analysis (Fig. 3a), all thermally-aged nanohybrids retained their original intense (001) Bragg reflections in the low angle region after the thermal aging process, confirming that the layer-by-layer ordering of the MoS_2 and RuO_2 NSs was retained. A closer inspection revealed that aging at 70°C

caused a slight but distinct displacement of the (001) peak toward the high angle region, providing strong evidence for shrinkage of interlayer distance and an enhancement in the interlayer interactions. In contrast, the crystal morphology and surface area showed only negligible variations caused by thermal aging, as evidenced by FE-SEM and N_2 adsorption–desorption isotherm measurements (Figs. S11 and S12, Supporting Information). These results strongly suggest that thermal aging has no significant influence on the stacking and pore structures of the restacked nanohybrids. According to the LSV measurements for the HER (Fig. 3c and Table S3 of Supporting Information), thermal aging of the TBMR nanohybrids led to a significant decrease in the overpotentials, thereby highlighting the usefulness of aging in optimizing the electrocatalytic performances. Among the various thermally-aged materials presented herein, TBMR11A exhibited the lowest overpotential of 118 mV at 10 mA cm^{-2} . The HER activity of TBMR11A is comparable to the recently reported excellent HER performances of MoS_2 -based materials, confirming the usefulness of the present strategy (Table S4 of Supporting Information). This improvement of the HER kinetics after aging at an elevated temperature was cross-confirmed by Tafel slope calculations, which indicated markedly depressed Tafel slopes for the thermally-aged derivatives. The smallest Tafel slope of 56.9 mV dec^{-1} occurred for TBMR11A, which is in good agreement with its best electrocatalytic performance (Fig. 3d and Table S3 of Supporting Information). The beneficial effect of thermal aging on the electrochemical

activities of the TBMR nanohybrids was further evidenced by the ECSA determination (Fig. 3e and Table S3 of Supporting Information). The thermally-aged TBMR7A, TBMR9A, and TBMR11A derivatives showed expanded ECSAs of 21.2, 30.5, and 37.2 cm^2 , respectively, which are notably greater than those of the as-prepared TBMR7, TBMR9, and TBMR11 homologs, which in turn results in improved HER activities. Considering the negligible effect of thermal aging on the surface area of the restacked NSs, the observed larger ECSAs for the thermally-aged nanohybrids could be ascribed to surface activation and the enhanced electrochemical activities of the surface sites. In addition, the EIS measurements demonstrated an improvement in the charge transfer kinetics upon thermal aging. More specifically, in the Nyquist plots (Fig. 3f and Table S3 of Supporting Information), the thermally-aged nanohybrids displayed smaller semicircle radius than those of the as-prepared materials, highlighting a lowering of the charge transfer resistance (R_{ct}) as a result of the thermal aging process. Among the present nanohybrids, the TBMR11A nanohybrid with the highest HER activity exhibited the smallest semicircle radius and the smallest R_{ct} of 33.3Ω , thereby confirming the enhanced charge transfer kinetics upon thermal aging (Table S3 of Supporting Information). This is attributable to the enhanced electronic coupling resulting from the conductive RuO_2 NS. These electrochemical characterizations demonstrate that thermal aging is effective in improving the electrochemical activities and electrocatalytic performances of restacked 2D inorganic NS-based hybrids.

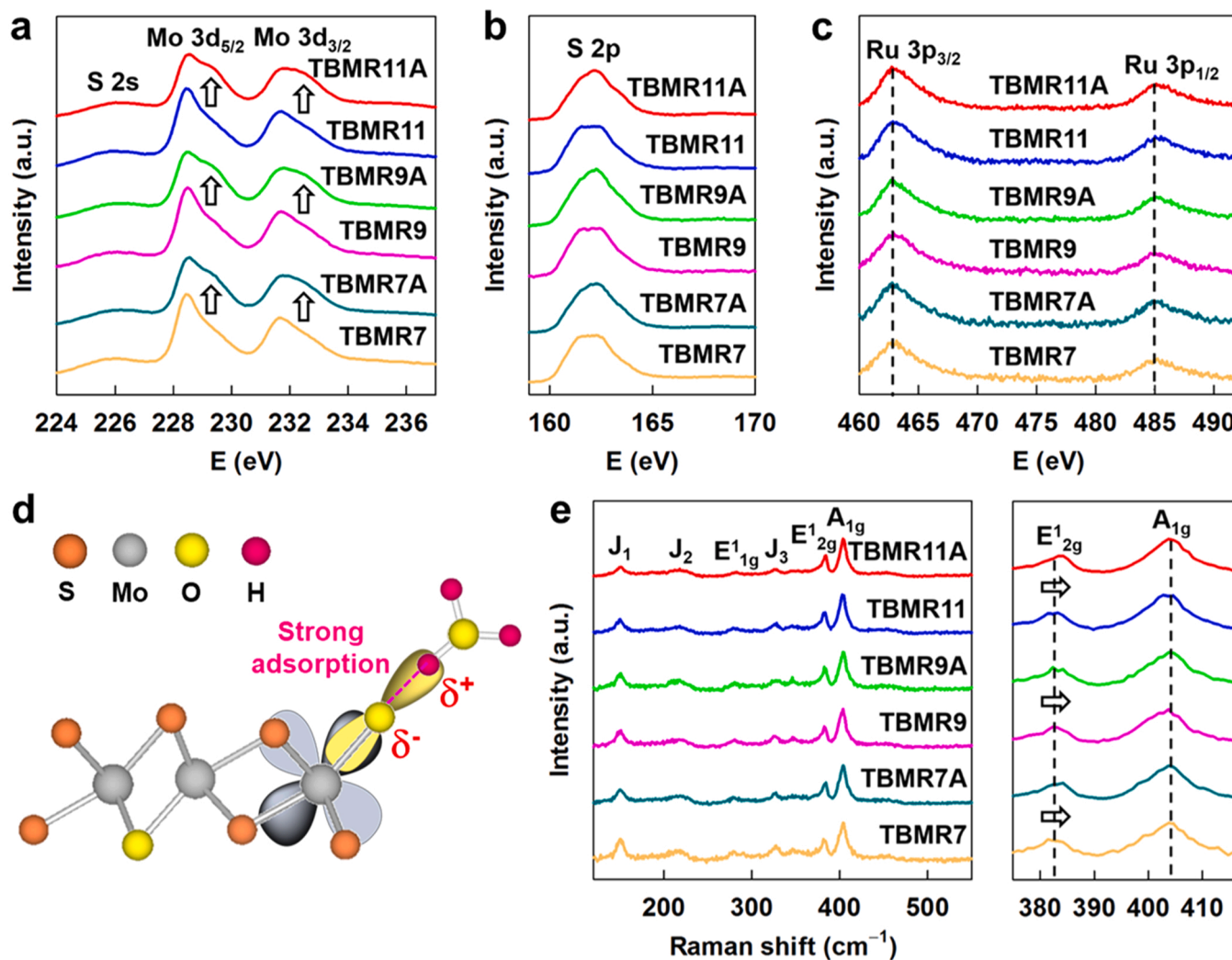


Fig. 4. (a) Mo 3d XPS, (b) S 2p XPS, (c) Ru 3p XPS, (d) Schematic model for the evolution of chemical bonding upon the thermal aging process, and (e) micro-Raman data of TBMR7, TBMR9, and TBMR11 before and after thermal aging process.

To examine the influence of the thermal aging conditions on the electrocatalytic performances of the **TBMR** nanohybrids, thermal aging was also carried out at a higher temperature of 90 °C and over longer aging times of 3 and 5 h. As presented in Fig. S14 of Supporting Information, these increases in the aging temperature and aging time were found to induce only slight degradations in the HER functionality. This result clearly demonstrates that a short aging process (i.e., 1 h) at a relatively mild temperature of 70 °C is optimal for the surface activation of monolayered TMD NSs.

3.5. Evolution of the chemical bonding nature of restacked MoS_2 - RuO_2 NSs upon thermal aging process

To understand the origin of this beneficial effect imparted by the thermal aging process, evolution of the chemical bonding natures of the restacked **TBMR** nanohybrids before and after thermal aging was investigated using a series of spectroscopic techniques. According to the Mo 3d XPS analysis (Fig. 4a), aging at 70 °C enhances the intensity of the high-energy shoulder peak, indicating the formation of highly oxidized Mo species that is possibly induced by the formation of (Mo–O) bonding with the significant transition to a 2 H- MoS_2 phase. According to the peak deconvolution analysis for the Mo 3d XPS data (Fig. S15, Supporting Information), the thermal aging process was found to increase the (Mo–O) component as well as 2 H- MoS_2 phase, thereby confirming the oxygenation of MoS_2 lattice and the phase transformation from 1 T'- MoS_2 to 2 H- MoS_2 . Similarly, in the S 2p XPS region (Fig. 4b and S16, Supporting Information), thermal aging resulted in an enhancement of the spectral weight for the high-energy component as well as a peak shift toward the high-energy side, thereby confirming the partial structural transition to the 2 H- MoS_2 phase. Taking into account the detrimental effect of the increase of 2 H- MoS_2 content on the HER electrocatalyst performance [46], the significant improvement of HER activity upon the thermal aging clearly demonstrated the overwhelming beneficial effect of oxygenation over the negative effect of 2 H- MoS_2 formation. Thus, this result can be regarded as strong evidence for the high efficacy of oxygenation in improving the HER electrocatalytic activity. In contrast to these MoS_2 -related spectral features, no marked spectral modification was observed in the Ru 3d region after thermal aging, which highlights the negligible effect of oxygenation on the RuO_2 layer (Fig. 4c). Thus, the present XPS results clearly demonstrate that oxygenation occurred predominantly in the MoS_2 layer and not in the RuO_2 layer. Such a partial oxygenation of the MoS_2 layer leads to diversification of the surface bonds via the formation of (Mo–O) bonds, which is beneficial in terms of enhancing the electrochemical activity of the MoS_2 NSs (Fig. 4d). Considering the remarkable increase in the ECSA and the negligible variation in the surface area after thermal aging, the oxidative surface activation of the MoS_2 layer was considered to be responsible for the increased ECSA values of the thermally-aged derivatives. Additionally, the enhancement of the MoS_2 NS bond polarity caused by partial oxygenation promotes interfacial electronic coupling with the restacked RuO_2 NSs via reinforcement of the dipole–dipole interactions, ultimately leading to a reduction in the charge transfer resistance during thermal aging. The profound effect of thermal aging on the chemical bonding character of the MoS_2 layer was further confirmed by micro-Raman spectroscopy. The phonon energies of the MoS_2 lattice become higher after thermal aging, thereby indicating the reinforcement of (Mo–S) bonding upon partial oxidation of the MoS_2 NS (Fig. 4e).

3.6. Crucial contributions of enhanced hydrogen adsorption and promoted Volmer–Tafel mechanism to improved HER activity of restacked MoS_2 - RuO_2 NSs

The variation in the chemical bonding character observed for the **TBMR** nanohybrids during the HER process was then investigated by *in-situ* surface-enhanced Raman spectroscopy (SERS) to understand the

origin of their improved HER activity, as depicted in Fig. 5a. It should be noted here that the *in-situ* SERS measurement is one of the most effective techniques in directly probing the influence of HER process on the chemical bonding of the **TBMR** nanohybrids (Fig. 5b). Before and after the application of an electrical potential, all materials retained the Raman spectral features corresponding to the 1 T'- MoS_2 phase [37], thereby confirming retention of the metallic 1 T'- MoS_2 lattice during the HER process (Fig. 5c–5e). A closer inspection revealed that the **TBMR11** and **TBMR11A** nanohybrids displayed a significant broadening of the A_{1g} mode related to the symmetric (Mo–S) vibration, which is caused by the increased spectral weight at the low wavenumber side. This observation reflects the weakening of (Mo–S) bond during the HER process. As illustrated in Fig. 5b, this spectral change can be interpreted as a result of proton adsorption on the MoS_2 lattice, resulting in the weakening of the adjacent (Mo–S) bonds. In contrast, there is no notable alteration of the A_{1g} peak width for the MoS_2 NS precursor upon the application of an electrical potential. The Raman results therefore provide strong evidence for enhanced proton adsorption in the **TBMR11** and **TBMR11A** nanohybrids during the HER process, which originates from the increased ECSA and surface reactivity. This makes a significant contribution to the improvement in HER activity via the enhanced adsorption and the resulting accumulation of hydrogen, promoting the Volmer–Tafel process.

In addition, *in-situ* Mo K-edge XANES analysis was further performed to elucidate the mechanism responsible for the improvement of HER activity. The **TBMR11** nanohybrid showed only a negligible change of the Mo K-edge position upon the application of a reductive potential, which is in stark contrast to the MoS_2 NS precursor that exhibits a decrease in its Mo K-edge energy during the HER process (Fig. 6a–c). The observed displacement of the Mo K-edge energy toward the low-energy side for the MoS_2 NS can be interpreted as a result of charge accumulation caused by the application of a reductive potential. Conversely, no significant change was observed for the Mo K-edge energy of **TBMR11** upon increasing the reductive potential, and this can be ascribed to efficient charge transfer to the adsorbed protons, which results in a negligible accumulation of the electronic charge during the HER process. This observation is in good agreement with higher HER activity of **TBMR11** compared to the MoS_2 NS. In the case of the thermally-aged **TBMR11A** nanohybrid, the increase in the reductive potential displaced the Mo K-edge position toward high-energy side. The detachment of numerous adsorbed hydrogen atoms at larger reductive potentials is responsible for the blue shift of the Mo K-edge position, since this process results in the significant lowering of the Mo ion electron density. This result implies the enhancement of hydrogen atom accumulation caused by thermal surface activation and the following detachment of numerous adsorbed hydrogen atoms at higher reductive potential in the **TBMR11A** nanohybrid. As described in Fig. 6d, the Volmer–Heyrovsky mechanism relies on the combination of adsorbed single hydrogen atom and hydrogen atom of water molecule in electrolyte, whereas the Volmer–Tafel mechanism occurs by the combination of two adsorbed hydrogen atoms. Thus, the enhanced adsorption of hydrogen atoms in the **TBMR11A** nanohybrid is more beneficial for the Volmer–Tafel process than for the Volmer–Heyrovsky process, since the accumulation of adsorbed hydrogen atoms on the catalyst surface facilitates the formation of H_2 molecules by the combination of two adsorbed hydrogen atoms (i.e., via the Volmer–Tafel process) [47]. Thus, the *in-situ* XANES results highlight that, in comparison with **TBMR11** nanohybrid with dominant contribution of the Volmer–Heyrovsky mechanism, the thermally-activated **TBMR11A** nanohybrid showed a larger contribution of the Volmer–Tafel process than the Volmer–Heyrovsky process to its improved HER activity (Fig. 6d).

3.7. Elucidating dominant design factors for high-performance 2D hybrid electrocatalysts

To establish a dominant design factor for the preparation of high-

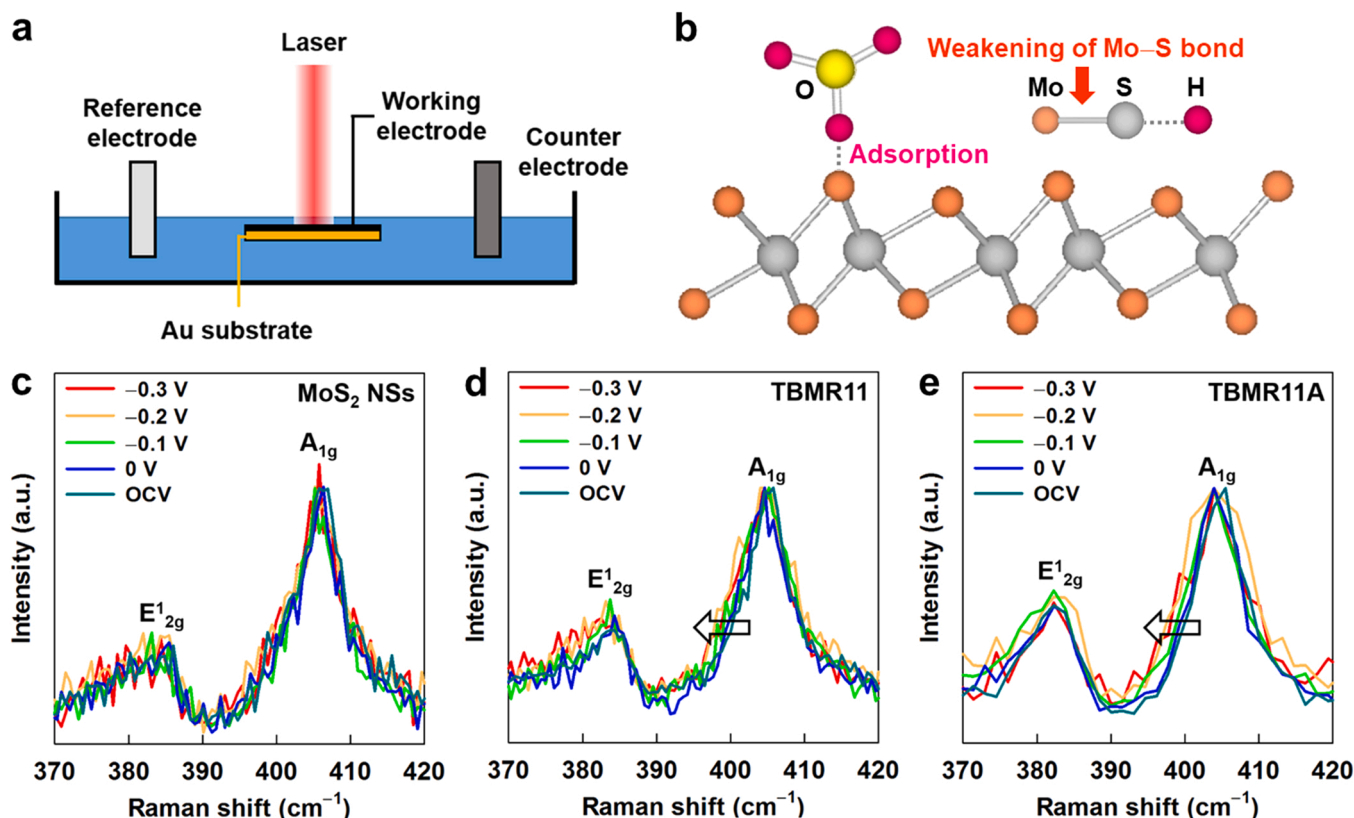


Fig. 5. (a) Experimental setup for *in-situ* SERS measurements, (b) schematic model for the effect of surface activation on chemical bonding and proton adsorption behavior, and *in-situ* SERS data of (c) MoS₂ NSs, (d) TBMR11, and (e) TBMR11A during the HER process.

performance 2D nanostructured electrocatalysts, the HER overpotentials of the restacked nanohybrids are plotted as a function of the interlayer distance, the defect content, the stacking thickness, the host composition, the (Mo–O) bond content, the ECSA, and the surface area. The HER activity of the restacked nanohybrid displayed a non-monotonous correlation with the interlayer distance between the MoS₂ and RuO₂ NSs (Fig. 7a). Among the present nanohybrids, a lower overpotential was observed upon restacking with TBA compared to those of the other cation-restacked homologs, thereby indicating that the optimal interlayer distance for improving the electrocatalyst performance was ~ 11.7 Å. This observation is in contrast to common conjecture, in which a gradual increase of the interlayer space leads to a continuous improvement of the HER activities of 2D TMD materials [48]. As shown in the plot of overpotential vs. defect content (Fig. 7b), all the present organic–MoS₂–RuO₂ nanohybrids except for **TEMR7** exhibited the increase of the HER overpotential with increasing the defect content of MoS₂ component, indicating the detrimental effect of crystal defects on the electrocatalytic performance. This finding strongly suggests that the MoS₂ NS possesses an excess concentration of crystal vacancies in terms of the achieving the optimal HER activity. Specifically, the **THMR7** nanohybrid does not have the most excellent HER electrocatalytic activity even with the highest defect concentration. Although the S vacancies can act as active sites for HER process, too high concentration of crystal defects degrades the charge transport properties, which has detrimental effect on the HER activity. Thus, the depression of charge transfer property caused by very high defect content of **THMR7** is responsible for its lower HER activity than **TBMR7** with optimal defect concentration. As found from EXAFS analysis, the defect content became larger with increasing the interlayer distance whereas the increase of the MoS₂/RuO₂ ratio led to the increase of sulfur vacancy concentration. Conversely, the ECSAs of the nanohybrids showed a superior linear relationship with the HER overpotential

compared to the other factors (Fig. 7c), highlighting the usefulness of the ECSA as dominant design factors for high-performance 2D electrocatalysts. An increase in the ECSA leads to an enhanced adsorption of protons, as confirmed by the *in-situ* SERS and XANES results, which indicate improvements in the degrees of proton adsorption and increased contribution of Volmer–Tafel mechanism via hydrogen accumulation. Furthermore, this result supports the usefulness of thermal aging in terms of optimizing the electrocatalytic performances of 2D nanostructured materials via surface activation. The ECSA showed a non-monotonous complex dependency on the interlayer space, because the basal expansion caused by the intercalation of bulky organic cations enhances the ECSA due to the increase of surface area and simultaneously the accompanying increase of electrochemically-inactive hydrophobic organic content depresses the ECSA of nanohybrid. As depicted in Fig. 7d, the increase of RuO₂/MoS₂ ratio resulted in the lowering of HER overpotential upto **TBMR11**, whereas a further increase of this ratio enhances the HER overpotential, underscoring the present of optimal RuO₂/MoS₂ ratio in improving the HER activity. In Fig. S17 of Supporting Information, the HER overpotential showed the distinct decrease with increasing the relative content of (Mo–O) bond caused by thermal aging, clearly demonstrating the crucial role of oxygenation in optimizing the HER performance. However, in contrast to the aforementioned factors, both the stacking thickness and the surface area showed poor correlations with the HER overpotential (Figs. 7e and 7f), clarifying that these parameters are not suitable as design factors for high-performance electrocatalysts. The stacking thickness does not show a straightforward relationship to the interlayer distance, which can be interpreted as an interplay among the non-monotonous variations of charge density and hydrophilicity/hydrophobicity of organic intercalant ions. In contrast, the increase of interlayer distance enhances the surface area of restacked nanohybrids whereas the thermal aging and RuO₂ introduction have negligible influence on the surface area of

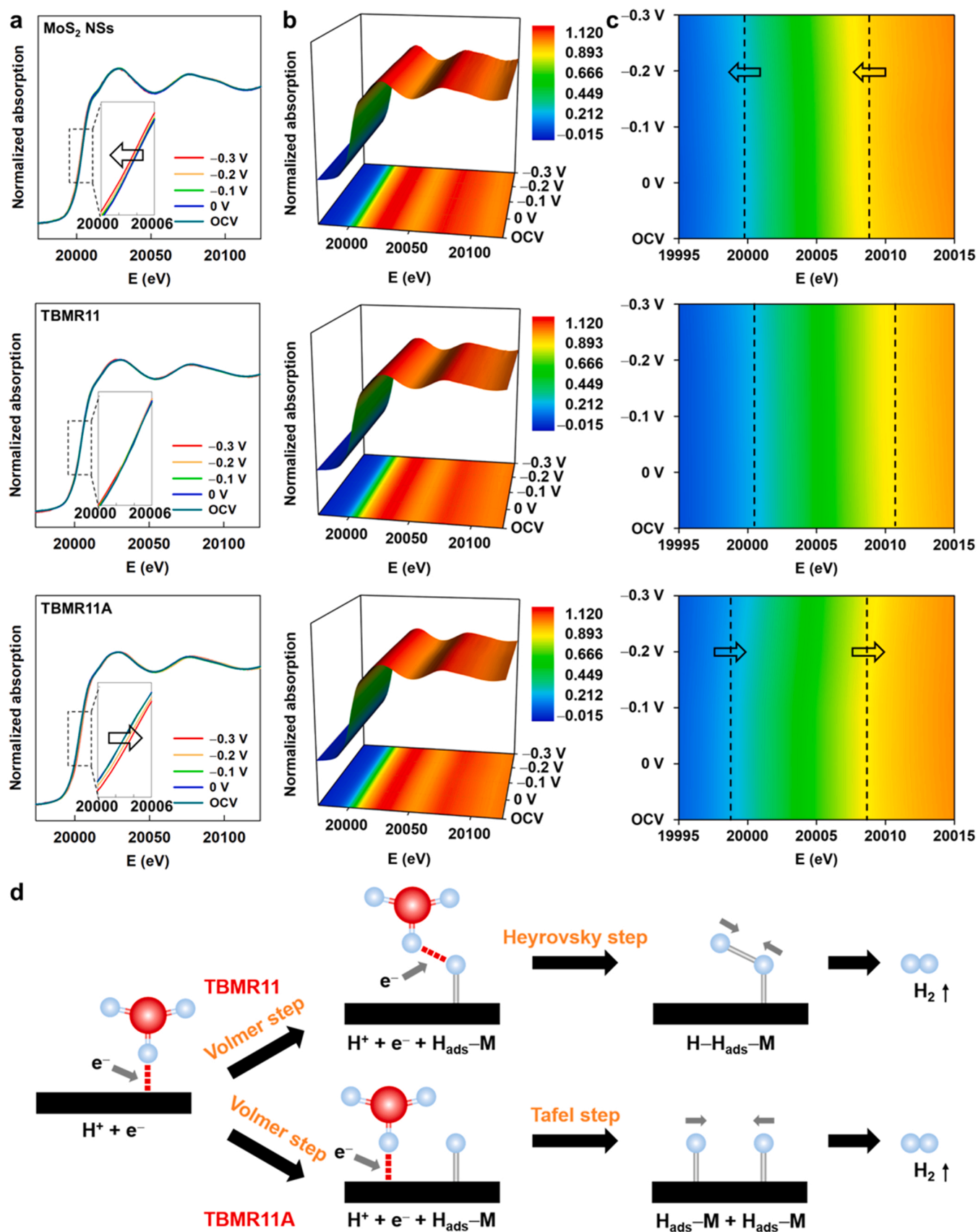


Fig. 6. (a) *In-situ* Mo K-edge XANES spectra, (b) 3D contour plots, and (c) 2D contour plots of rising edge regions of MoS₂ NSs, TBMR11, and TBMR11A during the HER process. (d) Schematic model for the interfacial charge transfer and HER mechanisms of TBMR11 nanohybrid before and after thermal aging process.

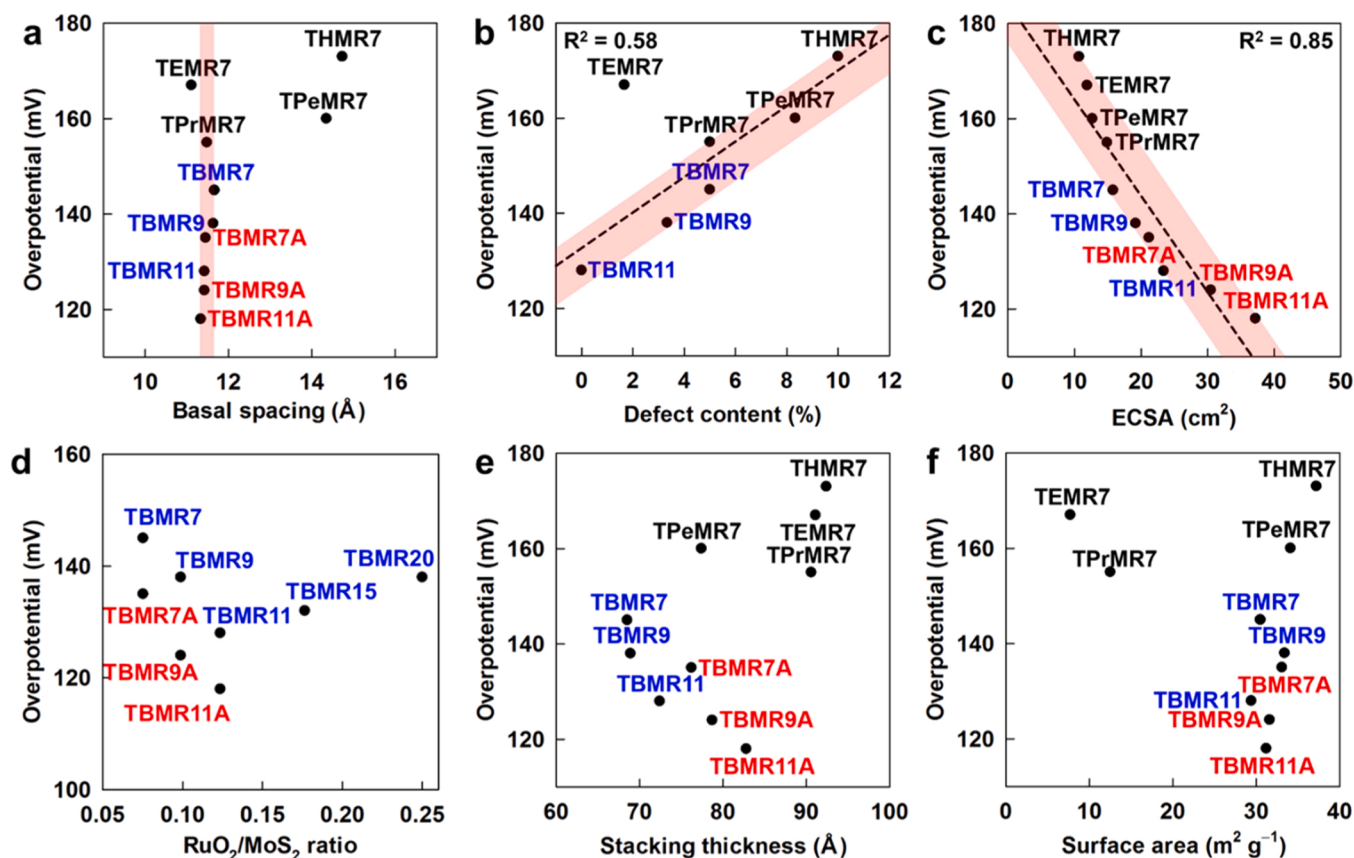


Fig. 7. Correlation plots of HER overpotential vs. (a) interlayer distance, (b) defect content, (c) ECSA, (d) $\text{RuO}_2/\text{MoS}_2$ ratio, (e) stacking thickness, and (f) surface area.

the present materials.

Based on the experimental findings presented herein, the beneficial effect of the synergetic combination of host–guest co-engineering and thermal aging on the HER electrocatalyst functionality can be ascribed to the following factors. Firstly, the partial oxygenation caused by the thermal aging process as well as the incorporation of polar RuO_2 NS enhances the electrochemical activity and surface bond polarity of nanohybrids. Since the introduction of surface oxygen species and the increase of surface polarity can enrich adsorption sites for the H^+ reaction intermediate [17], both the oxygenation of the MoS_2 NS and the

incorporation of polar RuO_2 NS can facilitate the energetically most unfavorable Volmer step of the HER process (i.e., $\text{H}_2\text{O} + \text{e}^- + \text{M}$ (active site) $\rightarrow \text{H}_{\text{ads}}-\text{M} + \text{OH}^-$), facilitating the Volmer–Tafel process. The increased contribution from the Volmer–Tafel mechanism due to an enhanced proton adsorptivity and an accumulation of adsorbed hydrogen atoms was evidenced by the *in-situ* SERS and XANES analyses. Second, the self-assembly of exfoliated MoS_2 and RuO_2 NSs with organic cations is effective in expanding the ECSA (Fig. 8) [49,50]. This increase in the ECSA is also responsible for the enhanced HER activities of the present nanohybrids. In addition, expansion of the interlayer space

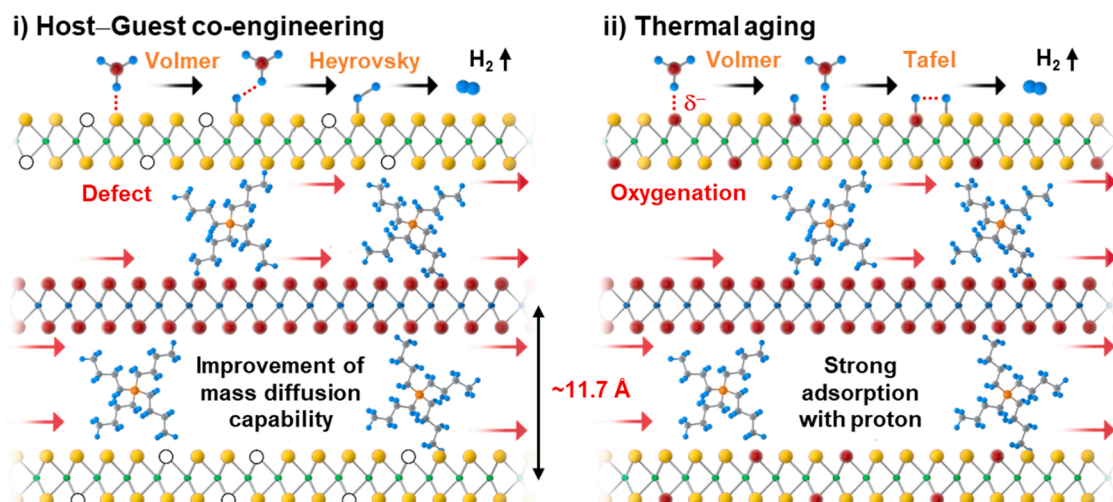


Fig. 8. Schematic model for the synergetic advantage of host–guest co-engineering and thermal aging in optimizing HER electrocatalyst performance.

following restacking with bulky TBA ions improves the mass diffusion capability, as evidenced by EIS measurement, while self-assembly with an organic species stabilizes the metallic 1T'-MoS₂ and RuO₂ phases, thereby further enhancing the HER activity *via* an improvement in the mass and charge transfer kinetics.

4. Conclusion

In this study, we elucidated a crucial role of promoted Volmer–Tafel mechanism in exploring high-performance two-dimensional (2D) nanostructured electrocatalysts, which was based on molecular-level control of the host, interlayer, and surface features. The synergetic combination of host–guest co-engineering and surface activation allowed to develop a novel lattice engineering strategy for the preparation of highly efficient hybrid electrocatalysts. Following thermal aging carried out in a standard glassware reactor, the restacked tetrabutylammonium (TBA)–MoS₂–RuO₂ nanohybrid with optimized guest and host structures delivered an excellent electrocatalyst performance for the hydrogen evolution reaction (HER) with a remarkably smaller overpotential (*i.e.*, ~118 mV) than those of the MoS₂ and RuO₂ nanosheet (NS) precursors and their physical mixture.

Additionally, the operation mechanism of the present restacked nanohybrids was clearly elucidated by combinative *in-situ* surface-enhanced Raman spectroscopy (SERS) and X-ray absorption near-edge structure (XANES) analyses. Based on these studies, the marked beneficial effect of the combinative host–guest co-engineering and thermal aging can be ascribed to the increased contribution of Volmer–Tafel process caused by the enhanced proton adsorption and adsorbed hydrogen accumulation as well as to the increase in the electrochemical active surface area (ECSA), and the improved charge/mass transport properties.

In addition, the systematic control of various structural and morphological parameters of the restacked NSs enabled us to understand their influences on the HER electrocatalyst performance of restacked nanohybrids. (1) First, the HER overpotentials of the restacked NSs were found to be well-correlated with the ECSA, underscoring the validity of the ECSA as a dominant design factor for exploring efficient 2D nanostructured electrocatalysts. The present study therefore confirms the efficiency of the thermal aging process in optimizing the electrocatalytic performances of 2D NS-based hybrid materials *via* oxidative surface activation. (2) Second, the variation of interlayer distance has significant influence on the HER activity. An interlayer distance of ~11.7 Å was found to be optimal for enhancing the electrocatalytic performance. (3) Third, the increase of the number of sulfur vacancies was found to induce the degradation of the HER activity. This result strongly suggests that the monolayer MoS₂ NS present in these nanohybrids is in the defect-over-doped state (*i.e.*, their defect content is too high). These results strongly suggest that the precise regulation of the defect concentration and the interlayer distance is critical to achieve the optimal electrocatalytic performances for 2D transition metal dichalcogenide (TMD) NSs. The present study clearly demonstrates that the molecular-level control of host, interlayer, and surface properties enables the design and synthesis of high-performance hybrid electrocatalysts.

Judging from the crucial roles of the surface activity and the charge/mass transport properties in determining the energy-related functionalities of such materials (*e.g.*, as photocatalysts and electrodes) [51–53], the described synthetic strategy could therefore provide a powerful means to explore high-performance energy-functional materials. Currently, we are examining the application of the above combinative synthetic strategy for optimizing the electrocatalytic performances of inorganic NSs for other reactions, including the oxygen evolution reaction (OER), the oxygen reduction reaction (ORR), and the nitrogen reduction reaction (NRR).

CRedit authorship contribution statement

Hyun Kyu Kim: Methodology, Validation, Formal analysis, Investigation, Visualization. **Haeseong Jang:** Methodology, Validation, Formal analysis, Investigation. **Xiaoyan Jin:** Conceptualization, Methodology, Validation, Formal analysis, Investigation, Visualization, Writing – review & editing, Supervision. **Min Gyu Kim:** Conceptualization, Methodology, Formal analysis, Investigation, Writing – review & editing, Supervision. **Seong-Ju Hwang:** Conceptualization, Methodology, Formal analysis, Investigation, Writing – original draft, Writing – review & editing, Supervision, Funding acquisition.

Declaration of Competing Interest

The authors declare that they have no known competing financial interests or personal relationships that could have appeared to influence the work reported in this paper.

Acknowledgement

This work was supported by the National Research Foundation of Korea (NRF) grant funded by the Korea government (MSIT) (No. NRF-2020R1A2C3008671, No. NRF-2017R1A5A1015365). This work was also supported by National R&D Program through the National Research Foundation of Korea (NRF) funded by Ministry of Science and ICT (No. 2021M3H4A1A03049662). The research was supported by the Yonsei University Research Fund of 2021-22-0304 and Yonsei Signature Research Cluster Program of 2021 (2021-22-0002). The experiments at PAL were supported in part by MOST and POSTECH.

Appendix A. Supporting information

Supplementary data associated with this article can be found in the online version at [doi:10.1016/j.apcatb.2022.121391](https://doi.org/10.1016/j.apcatb.2022.121391).

References

- [1] K. Kodama, T. Nagai, A. Kuwaki, R. Jinnouchi, Y. Morimoto, Challenges in applying highly active Pt-based nanostructured catalysts for oxygen reduction reactions to fuel cell vehicles, *Nat. Nanotechnol.* 16 (2021) 140.
- [2] T. Sun, S. Mitchell, J. Li, P. Lyu, X. Wu, J. Pérez-Ramírez, J. Lu, Design of local atomic environments in single-atom electrocatalysts for renewable energy conversions, *Adv. Mater.* 33 (2021), 2003075.
- [3] A. Saad, D. Liu, Y. Wu, Z. Song, Y. Li, T. Najam, K. Zong, P. Tsiakaras, X. Cai, Ag nanoparticles modified crumpled borophene supported Co₃O₄ catalyst showing superior oxygen reaction (OER) performance, *Appl. Catal. B Environ.* 298 (2021), 120529.
- [4] H. Wang, Y. Cui, Nanodiamonds for energy, *Carbon Energy* 1 (2019) 13.
- [5] W. Wu, M. Wang, H. Huang, W. Gu, C. Yan, G. Chen, D. Yin, H. Jin, J. Wang, S. Wang, Porous carbon spheres with ultra-fine Fe₂N active phase for efficient electrocatalytic oxygen reduction, *J. Electron. Mater.* 50 (2021) 3078.
- [6] X. Jin, T.-H. Gu, K.-G. Lee, M.-J. Kim, M.-S. Islam, S.-J. Hwang, Unique advantages of 2D inorganic nanosheets in exploring high-performance electrocatalysts: synthesis, application, and perspective, *Coord. Chem. Rev.* 415 (2020), 213280.
- [7] N.H. Kwon, S.-J. Shin, X. Jin, Y. Jung, G.-S. Hwang, H. Kim, S.-J. Hwang, Monolayered g-C₃N₄ nanosheet as an emerging cationic building block for bifunctional 2D superlattice hybrid catalysts with controlled defect structures, *Appl. Catal. B Environ.* 277 (2021), 119191.
- [8] N.H. Attanayake, A.C. Thenuwara, A. Patra, Y.V. Aulin, T.M. Tran, H. Chakraborty, E. Borguet, M.L. Klein, J.P. Perdew, D.R. Strongin, Effect of intercalated metals on the electrocatalytic activity of 1T'-MoS₂ for the hydrogen evolution reaction, *ACS Energy Lett.* 3 (2018) 7.
- [9] K. Zhang, P. Li, S. Guo, J.-Y. Jeong, B. Jin, X. Li, S. Zhang, H. Zeng, J.H. Park, An Ångström-level d-spacing controlling synthetic route for MoS₂ towards stable intercalation of sodium ions, *J. Mater. Chem. A* 6 (2018) 22513.
- [10] T.-H. Gu, X. Jin, S.-J. Park, M.G. Kim, S.-J. Hwang, Molecular-level control of the intersheet distance and electronic coupling between 2D semiconducting and metallic nanosheets: establishing design rules for high-performance hybrid photocatalysts, *Adv. Sci.* 8 (2021), 2004530.
- [11] X. Jin, S.-J. Shin, J. Kim, N.-S. Lee, H. Kim, S.-J. Hwang, Heterolayered 2D nanohybrids of uniformly stacked transition metal dichalcogenide–transition metal oxide monolayers with improved energy-related functionalities, *J. Mater. Chem. A* 6 (2018) 15237.
- [12] N. Kim, T.-H. Gu, D. Shin, X. Jin, H. Shin, M.G. Kim, H. Kim, S.-J. Hwang, Lattice engineering to simultaneously control the defect/stacking structures of layered

- double hydroxide nanosheets to optimize their energy functionalities, *ACS Nano* 15 (2021) 8306.
- [13] X. Jin, T.-H. Gu, N.H. Kwon, S.-J. Hwang, Synergetic advantages of atomically coupled 2D inorganic and graphene nanosheets as versatile building blocks for diverse functional nanohybrids, *Adv. Mater.* 33 (2021), 2005922.
 - [14] Z. Fan, Y. Wang, Z. Xie, D. Wang, Y. Yuan, H. Kang, B. Su, Z. Cheng, Y. Liu, Modified MXene/Holey graphene films for advanced supercapacitor electrodes with superior energy storage, *Adv. Sci.* 5 (2018), 1800750.
 - [15] M. Zhang, L. Zou, C. Yang, Y. Chen, Z. Shen, Z. Shen, C. Bo, An all-nanosheet OER/ORR bifunctional electrocatalyst for both aprotic and aqueous Li-O₂ batteries, *Nanoscale* 11 (2019) 2855.
 - [16] X. Jin, S.-J. Shin, N. Kim, B. Kang, H. Piao, J.-H. Choy, H. Kim, S.-J. Hwang, Superior role of MXene nanosheet as hybridization matrix over graphene in enhancing interfacial electronic coupling and functionalities of metal oxide, *Nano Energy* 53 (2018) 841.
 - [17] J. Petó, T. Ollár, P. Vancsó, Z.I. Popov, G.Z. Magda, G. Dobrik, C. Hwang, P. B. Sorokin, L. Tapasztó, Spontaneous doping of the basal plane of MoS₂ single layers through oxygen substitution under ambient conditions, *Nat. Chem.* 10 (2018) 1246.
 - [18] N. Luo, C. Chen, D. Yang, W. Hu, F. Dong, S defect-rich ultrathin 2D MoS₂: the role of S point-defects and S stripping-defects in the removal of Cr(VI) via synergistic adsorption and photocatalysis, *Appl. Catal. B Environ.* 299 (2021), 120664.
 - [19] F. Gong, S. Ye, M. Liu, J. Zhang, L. Gong, G. Zeng, E. Meng, P. Su, K. Xie, Y. Zhang, J. Liu, Boosting electrochemical oxygen evolution over yolk-shell structured O-MoS₂ nanoreactors with sulfur vacancy and decorated Pt nanoparticles, *Nano Energy* 78 (2020), 105284.
 - [20] A. Liu, L. Zhao, J. Zhang, L. Lin, H. Wu, Solvent-assisted oxygen incorporation of vertically aligned MoS₂ ultrathin nanosheets decorated on reduced graphene oxide for improved electrocatalytic hydrogen evolution, *ACS Appl. Mater. Interfaces* 8 (2016) 25210.
 - [21] Z. Wu, X. Zhang, D. Xu, J. Ge, Construction of nitrogen-doped carbon nanosheets for efficient and stable oxygen reduction electrocatalysis, *J. Electron. Mater.* 50 (2021) 1349.
 - [22] H. Song, M. Wu, Z. Tang, J.S. Tse, B. Yang, S. Lu, Single atom ruthenium-doped CoP/CDs nanosheets via splicing of carbon-dots for robust hydrogen production, *Angew. Chem. Int. Ed.* 60 (2021) 7234.
 - [23] W. Li, Y. Zhao, Y. Liu, M. Sun, G.I.N. Waterhouse, B. Huang, K. Zhang, T. Zhang, S. Lu, Exploiting Ru-induced lattice strain in CoRu nanoalloys for robust bifunctional hydrogen production, *Angew. Chem. Int. Ed.* 60 (2021) 3290.
 - [24] H. Song, Y. Li, L. Shang, Z. Tang, T. Zhang, S. Lu, Designed controllable nitrogen-doped carbon-dots-loaded MoP nanoparticles for boosting hydrogen evolution reaction in alkaline medium, *Nano Energy* 72 (2020), 104730.
 - [25] H.S.S. Ramakrishna Matte, A. Gomathi, A.K. Manna, D.J. Late, R. Datta, S.K. Pati, C.N.R. Rao, MoS₂ and WS₂ analogues of graphene, *Angew. Chem. Int. Ed.* 49 (2010) 4059.
 - [26] K. Fukuda, T. Saida, J. Sato, M. Yonezawa, Y. Takasu, W. Sugimoto, Synthesis of nanosheet crystallites of ruthenate with an α -NaFeO₂-related structure and its electrochemical supercapacitor property, *Inorg. Chem.* 49 (2010) 4391.
 - [27] P. Xiong, X. Zhang, H. Wan, S. Wang, Y. Zhao, J. Zhang, D. Zhou, W. Gao, R. Ma, T. Sasaki, G. Wang, Interface modulation of two-dimensional superlattices for efficient overall water splitting, *Nano Lett.* 19 (2019) 4518.
 - [28] S.-J. Hwang, C.-W. Kwon, J. Portier, G. Campet, H.-S. Park, J.-H. Choy, P.V. Huong, M. Yosahiro, M. Kakihana, Local crystal structure around manganese in new potassium-based nanocrystalline manganese oxyiodide, *J. Phys. Chem. B* 106 (2002) 4053.
 - [29] M. Ghidui, S. Kota, J. Halim, A.W. Sherwood, N. Nedfors, J. Rosen, V.N. Mochalin, M.W. Barsoum, Alkylammonium cation intercalation into Ti₃C₂ (MXene): effects on properties and ion-exchange capacity estimation, *Chem. Mater.* 29 (2017) 1099.
 - [30] L.Y. Yang, G.P. Feng, T.X. Wang, J.M. Zhang, T.J. Lou, Low temperature preparation and characterization of CdTiO₃ nanoplates, *Mater. Lett.* 65 (2011) 2601.
 - [31] K.E. Dungey, M.D. Curtis, J.E. Penner-Hahn, Structural characterization and thermal stability of MoS₂ intercalation compounds, *Chem. Mater.* 10 (1998) 2152.
 - [32] L. Wang, X. Zhang, Y. Xu, C. Li, W. Liu, S. Yi, K. Wang, X. Sun, Z.S. Wu, Y. Ma, Tetraethylammonium-intercalated 1T-MoS₂ nanosheets with expanded interlayer spacing vertically coupled on 2D delaminated MXene for high-performance lithium-ion capacitors, *Adv. Funct. Mater.* 31 (2021), 2104286.
 - [33] C. Zhao, J.M. Ang, Z. Liu, X. Lu, Alternately stacked metallic 1T-MoS₂/polyaniline heterostructure for high-performance supercapacitors, *Chem. Eng. J.* 330 (2017) 462.
 - [34] S. Maiti, K. Maiti, M.T. Curnan, K. Kim, K.-J. Noh, J.W. Han, Engineering electrocatalyst nanosurfaces to enrich the activity by inducing lattice strain, *Energy Environ. Sci.* 14 (2021) 3717.
 - [35] H. Li, C. Tsai, A.L. Koh, L. Cai, A.W. Contryman, A.H. Fragapane, J. Zhao, H.S. Han, H.C. Manoharan, F. Abild-Pedersen, J.K. Nørskov, X. Zheng, Activating and optimizing MoS₂ basal planes for hydrogen evolution through the formation of strained sulphur vacancies, *Nat. Mater.* 15 (2016) 48.
 - [36] S.J.R. Tan, S. Sarkar, X. Zhao, X. Luo, Y.Z. Luo, S.M. Poh, I. Abdelwahab, W. Zhou, T. Venkatesan, W. Chen, S.Y. Quek, K.P. Loh, Temperature- and phase-dependent phonon renormalization in 1T'-MoS₂, *ACS Nano* 12 (2018) 5051.
 - [37] B. Zong, Q. Xu, Q. Li, X. Fang, X. Chen, C. Liu, J. Zang, Z. Bo, S. Mao, Novel insights into the unique intrinsic sensing behaviors of 2D nanomaterials for volatile organic compounds: from graphene to MoS₂ and black phosphorous, *J. Mater. Chem. A* 9 (2021) 14411.
 - [38] M.-R. Gao, M.K.Y. Chan, Y. Sun, Edge-terminated molybdenum disulfide with a 9.4-Å interlayer spacing for electrochemical hydrogen production, *Nat. Commun.* 6 (2015) 7493.
 - [39] C.C.L. McCrory, S. Jung, J.C. Peters, T.F. Jaramillo, Benchmarking heterogeneous photocatalysts for the oxygen evolution reaction, *J. Am. Chem. Soc.* 135 (2013) 16977.
 - [40] C.C.L. McCrory, S. Jung, I.M. Ferrer, S.M. Chatman, J.C. Peters, T.F. Jaramillo, Benchmarking hydrogen evolving reaction and oxygen evolving reaction electrocatalysts for solar water splitting devices, *J. Am. Chem. Soc.* 137 (2015) 4347.
 - [41] G. Dong, M. Fang, H. Wang, S. Yip, H.-Y. Cheung, F. Wang, C.-Y. Wong, S.T. Chu, J. C. Ho, Insight into the electrochemical activation of carbon-based cathodes for hydrogen evolution reaction, *J. Mater. Chem. A* 3 (2015) 13080.
 - [42] N.H. Kwon, X. Jin, S.-J. Kim, H. Kim, S.-J. Hwang, Multilayer conductive hybrid nanosheets as versatile hybridization matrices for optimizing the defect structure, structural ordering, and energy-functionality of nanostructured materials, *Adv. Sci.* 9 (2022), 2103042.
 - [43] C. Wang, L. Qi, Heterostructured inter-doped ruthenium-cobalt oxide hollow nanosheet arrays for highly efficient overall water splitting, *Angew. Chem. Int. Ed.* 59 (2020) 17219.
 - [44] S. Brem, K.-Q. Lin, R. Gillen, J.M. Bauer, J. Maultzsch, J.M. Lupton, E. Malic, Hybridized intervalley Moiré excitons and flat bands in twisted WSe₂ bilayers, *Nanoscale* 12 (2020) 11088.
 - [45] S.-Y. Seo, D.-H. Yang, G. Moon, O.F.N. Okello, M.Y. Park, S.-H. Lee, S.-Y. Choi, M.-H. Jo, Identification of point defects in atomically thin transition-metal dichalcogenide semiconductors as active dopants, *Nano Lett.* 21 (2021) 3341.
 - [46] D. Wang, X. Zhang, S. Bao, Z. Zhang, H. Fei, Z. Wu, Phase engineering of a multiphase 1T/2H MoS₂ catalyst for highly efficient hydrogen evolution, *J. Mater. Chem. A* 5 (2017) 268.
 - [47] J. Lee, J. Heo, H.Y. Lim, J. Seo, Y. Kim, J. Kim, U. Kim, Y. Choi, S.H. Kim, Y. J. Yoon, T.J. Shin, J. Kang, S.K. Kwak, J.Y. Kim, H. Park, Defect-induced in situ atomic doping in transition metal dichalcogenides via liquid-phase synthesis toward efficient electrochemical activity, *ACS Nano* 14 (2020) 17114.
 - [48] J. Xu, Y. Huang, X. Cheng, T. Liu, Y. Lu, X. Chen, Y. You, J. Zhang, Interlayer-expanded and defect-rich metal dichalcogenide (MX₂) nanosheets for active and stable hydrogen evolution, *Inorg. Chem. Front.* 5 (2018) 3140.
 - [49] X. Jin, D.A. Agyeman, S. Kim, Y.H. Kim, M.G. Kim, Y.-M. Kang, S.-J. Hwang, Crucial roles of interfacial coupling and oxygen defect in multifunctional 2D inorganic nanosheets, *Nano Energy* 67 (2020), 104192.
 - [50] S. Venkateshwaran, M.J. Josline, S.M. Senthil Kumar, Fine-tuning interlayer spacing in MoS₂ for enriching 1T phase via alkylated ammonium ions for electrocatalytic hydrogen evolution reaction, *Int. J. Hydrog. Energy* 46 (2021) 8377.
 - [51] Y.K. Jo, J.M. Lee, S. Son, S.-J. Hwang, 2D inorganic nanosheet-based hybrid photocatalysts: design, applications, and perspectives, *J. Photochem. Photobiol. C Photochem. Rev.* 40 (2019) 150.
 - [52] Y. Song, B. Xu, T. Liao, J. Guo, Y. Wu, Z. Sun, Electronic structure tuning of 2D metal(Hydro)oxides nanosheets for electrocatalysis, *Small* 17 (2021), 2002240.
 - [53] T.-H. Gu, N.H. Kwon, K.-G. Lee, X. Jin, S.-J. Hwang, 2D inorganic nanosheets as versatile building blocks for hybrid electrode materials for supercapacitor, *Coord. Chem. Rev.* 421 (2020), 213439.